

Incomplete Multimodal Industrial Anomaly Detection via Cross-Modal Distillation

Wenbo Sui^{12*}, Daniel Lichau¹, Josselin Lefèvre¹³ Harold Phelippeau¹

¹Thermo Fisher Scientific

²Technical University of Denmark

³Univ Gustave Eiffel, CNRS, LIGM

websui@dtu.com, {daniel.lichau, josselin.lefevre, harold.phelippeau}@thermofisher.com

<https://github.com/evenrose/CMDIAD>

Abstract

Recent studies of multimodal industrial anomaly detection (IAD) based on 3D point clouds and RGB images have highlighted the importance of exploiting the redundancy and complementarity among modalities for accurate classification and segmentation. However, achieving multimodal IAD in practical production lines remains a work in progress. It is essential to consider the trade-offs between the costs and benefits associated with the introduction of new modalities, while ensuring compatibility with current processes. Existing quality control processes combine rapid in-line inspections, such as optical, infrared and ultrasound imaging with high-resolution but time-consuming near-line characterization techniques, including industrial CT, X-ray scattering and electron microscopy to manually or semi-automatically locate and analyze defects in the production of Li-ion batteries and composite materials. Given the cost and time limitations, only a subset of the samples can be inspected by all in-line and near-line methods, and the remaining samples are only evaluated through one or two forms of in-line inspection. To fully exploit data for deep learning-driven automatic defect detection, the models must have the ability to leverage multimodal training and handle incomplete modalities during inference. In this paper, we propose **CMDIAD**, a Cross-Modal Distillation framework for IAD to demonstrate the feasibility of a Multi-modal Training, Few-modal Inference (MTFI) pipeline. Our findings show that the MTFI pipeline can more effectively utilize incomplete multimodal information compared to applying only a single modality for training and inference. Moreover, we investigate the reasons behind the asymmetric performance improvement using point clouds or RGB images as the main modality of inference. This provides a foundation for our future multimodal dataset construction with additional modalities from manufacturing scenarios.

Introduction

Industrial anomaly detection (IAD) aims to detect abnormal characteristics of products during or after the manufacturing process to minimize the risk of potential defects. The rapid development of deep learning-based image IAD has led to more accurate and robust detection and moved away from handcrafted feature engineering to learn more complex patterns for variable issues (Liu et al. 2024; Tao et al. 2022). As a data-driven method, whether the input of the model can provide sufficient defect-related information determines the upper limit of the performance.

For example, 3D anomaly detection based on Point Clouds (PCs) input can capture unique spatial information of defects compared with RGB images but also loses sensitivity to color (Bergmann and Sattlegger 2023). Therefore, taking advantage of the redundancy and complementary between modalities is crucial for IAD. The recent studies on multimodal IAD (Costanzino et al. 2023; Rudolph et al. 2023; Wang et al. 2023b) demonstrate the superiority of multimodal input based on a benchmark dataset, MVTec 3D-AD (Bergmann et al. 2022), which introduced aligned 3D PCs and RGB images as complementary modalities.

Nevertheless, achieving multimodal IAD in practical production lines remains a work in progress. It requires consideration of the trade-offs between the costs and benefits associated with the introduction of new modalities, while ensuring compatibility with existing processes. The current production of Li-ion batteries and composites integrate rapid in-line inspections, such as optical, infrared, X-ray and ultrasound imaging with high-resolution but time-consuming near-line characterization techniques, including industrial CT, X-ray scattering and electron microscopy to manually or semi-automatically analyze anomalies (Reynolds et al. 2021; Fu and Yao 2022). Due to cost and time constraints, only a subset of samples can be inspected by all in-line and near-line methods, and the remaining samples are evaluated by only one or two forms of in-line inspection. To fully exploit data for deep learning-driven automatic defect detection, the models must have the ability to leverage multimodal training and handle incomplete modalities during inference. In a related study field, medical anomaly detection, Cao et al. (2023) achieved excellent results by applying the knowledge learned from high-resolution contrast-enhanced CT to common rapid non-contrast CT as a tool for early screening of pancreatic cancer and demonstrated the possibility of effective cross-modal enhancement. In the case of IAD, if limited results of one in-line or near-line modality can be used to leverage another in-line method, superior performance can be achieved with minimal additional cost.

To solve missing modality issues from real world in multimodal learning domain, researchers have tried to apply cross-modal Knowledge Distillation (KD) to deal with missing information more robustly in audio tagging (Yin et al. 2021), action recognition (Garcia, Morerio, and Murino 2018), medical image segmentation (Wang et al. 2023a), and

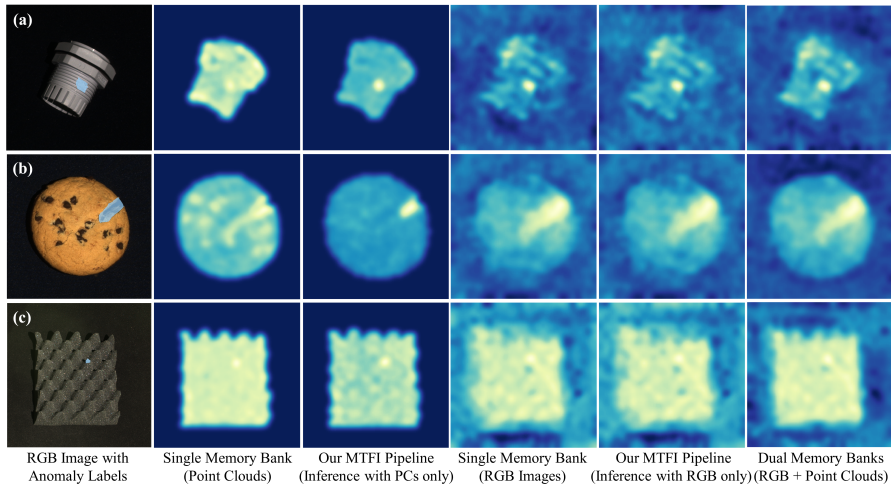


Figure 1: Qualitative comparison of prediction results of Multi-modal Training, Few-modal Inference (MTFI) pipeline (Feature-to-Feature), single memory bank (one modality for both training and inference), and dual memory banks (RGB+PCs for training and inference) on: (a) Cable Gland-Thread-013, (b) Cookie-Crack-003 and (c) Foam-Contamination-01 of MVTec 3D-AD.

saliency detection (Wang et al. 2022), etc. In contrast with the typical KD approaches, which involve teacher and student networks that accept the same modal input, the cross-modal KD’s student network attempts to generate the same output as the teacher based on additional modalities. In other words, cross-modal KD is capable of estimating the missing information based on the known modalities by establishing a mapping between one modality and another. This inspires us to enhance the unsupervised IAD method through cross-modal KD to develop a Multi-modal Training, Few-modal Inference (MTFI) pipeline which enables the model to be trained with data from multiple inspection methods but perform inference with only one of them.

In this paper, we propose **CMDIAD**, a Cross-Modal Distillation framework for IAD that learns to generate cross-modal hallucinations of missing modalities, with the objective of investigating the feasibility of the MTFI pipeline and what information can be transferred across modalities. We adopted the unsupervised Memory Bank method from (Wang et al. 2023b; Roth et al. 2022) as the foundation. The core idea of our framework is to train learnable cross-modal KD networks to emulate the privileged information (Vapnik and Vashist 2009a) like features or inputs of a given modality that is only present in the training phase and then try to generate its missing information during the inference phase. To show its potential, we tested the framework feeding in 3D PCs information to generate RGB information on MVTec 3D-AD (Bergmann, et al. 2022) dataset. The MTFI pipeline with Feature-to-Feature (F2F) network shows most promising improvement compared with the single 3D PCs memory bank model (Figure 1), and even exceeds the results of the SOTA Shape-guided model (Chu et al. 2023) with PCs input only, which combines PointNet (Qi et al. 2017) and Neural Implicit Function (Qian et al. 2022). This once again shows the importance of multi-modal information and proves the feasibility of our pipeline. Interestingly, when we reverse the distillation direction and re-

train the model to perform inference using RGB information and the PCs hallucination generated by the cross-modal KD networks, the performance improvement is either minimal or even declines. We further visualized and manually inspected the inputs and predictions, and attribute this asymmetry to the similar texture information between PCs and RGB images and the unique spatial information of PCs that cannot be estimated. These findings suggest that when constructing a multimodal IAD dataset in the future, it would be prudent to prioritize the use of in-line and near-line methods with associated information, because the MTFI pipeline based on cross-modal KD can only enhance the utilization of incomplete multimodal information instead of generating non-existent abnormal features as if by magic. The key contributions of our work are as follows:

- To the best of our knowledge, we are the first to implement IAD using incomplete multimodal data, which fits the actual scenario in the quality control process.
- We propose CMDIAD, a novel multimodal IAD framework which enables the model to be trained with multimodal data but perform inference with only one method.
- Our results illustrate the importance of associated information across modalities for incomplete multimodal IAD, and provide guidance for the selection of in-line and near-line methods for future dataset construction.

Related Work

Unsupervised 2D Industrial Anomaly Detection. Current research of 2D IAD focuses on unsupervised methods based on feature embeddings or reconstruction (Liu et al. 2024). The key of feature-embedding based methods is to translate normal samples into feature embeddings, and make specific comparison among the generated features, *e.g.*, the teacher-student architecture (Rudolph et al. 2023; Salehi et al. 2021) determines the anomaly scores by measuring

the distance between the teacher and student network outputs which relies on the teacher pre-trained on large dataset. There are also similar methods through one-class classification (Yoa et al. 2021; de Haan and Löwe 2021) and feature distribution map (Tailanian, Musé, and Pardo 2021; Kim et al. 2022). Memory bank methods select and save the anomaly-free feature from the pre-trained network to form a memory, and then compare the features of test samples with the memory, which improves the recall (Roth et al. 2022; Lee, Lee, and Song 2022; Zou et al. 2022). Reconstruction based methods apply Auto-encoder (AE) (Bergmann et al. 2018; Wang et al. 2020b), Generative Adversarial Networks (GAN) (Yan et al. 2021; Liang et al. 2023), or Diffusion Model (Wyatt et al. 2022; Teng et al. 2022) and force the model to reconstruct normal samples. Since the model does not have the knowledge to reconstruct the abnormal part, the output of the abnormal sample will be partially dissimilar compared with the input, as a sign of anomalies.

3D and Multi-modal RGB-3D Industrial Anomaly Detection. The first public RGB-3D industrial anomaly detection dataset from real-world objects, MVTEC 3D-AD (Bergmann et al. 2022), has greatly promoted studies in this field. AST (Rudolph et al. 2023) applied asymmetric teacher-student networks with RGB and depth map as inputs to avoid student learning anomalies through generalization. Horwitz and Hoshen (2023) improved the utilization of spatial information by handcrafted and learned shape representations. A memory bank method, M3DM (Wang et al. 2023b), replaced RGB and hand-crafted 3D features with frozen feature extractors pre-trained on large datasets like ImageNet (Deng et al. 2009) and generate fused features by forcing the output of additional learnable modules to be similar. Inspired by the adoption of feature extractors, Costanzino et al. (2023) built a cross-modal mapping module and evaluated the anomaly score through comparing fake features with the real features. Since the features obtained from pre-trained extractors are independent which leads to difficulties in modality fusion, DADA (Zavrtanik, Kristan, and Skočaj 2024) learned a joint representation of RGB-3D inputs by retraining the RGB backbone, resulting in enhanced detection performance.

Cross-modal Knowledge Distillation. Most existing multimodal architectures require complete modalities for both training and inference, which limits their applicability in the real world with missing modalities (Sun et al. 2023). Cross-modal KD is regarded as an effective method for missing modalities as its ability to transfer knowledge between different modalities. This method is also regarded as learning with privileged information in previous research (Vapnik 2006; Vapnik and Vashist 2009b), which means that some additional information (extra modalities) related to the training examples will be provided to the teacher, while this privileged information will not be available during inference. Garcia, Morerio, and Murino (2018) employed hallucination network as the student model to generate RGB-D cross-modal hallucination for video action recognition. Wang et al. (2023a) proposed LCKD to handle missing modalities through identifying the most important modality

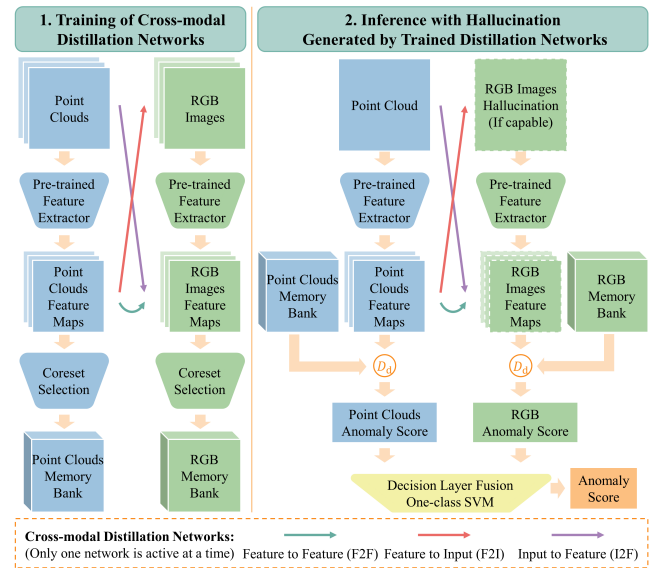


Figure 2: A conceptual illustration of two stages of MTFI pipeline (Inference with PCs only).

as a teacher. Previous research focused more on how to complete training in missing modalities with enhanced performance and lacked investigation into the correlation between modalities. However, inferring the latter through experimental results is more important because it can guide how to use existing modalities in quality control and the prior knowledge of human experts to improve the final defect detection rate of multimodal IAD.

Method

Our Cross-Modal Distillation framework for IAD (CM-DIAD) introduces a Multi-modal Training and Few-modal Inference (MTFI) pipeline as the basis of being compatible with single-modal training, single-modal inference and multi-modal training, multi-modal inference workflows. As shown in Figure 2, this is achieved by: 1) frozen pre-trained networks for feature extraction of pre-processed RGB images and PCs; 2) coreset selection module for memory bank construction; 3) cross-modal distillation network to generate hallucination of one modality from another modality to compensate missing information during inference; 4) decision layer fusion module to utilize multiple memory banks for classification and segmentation.

Feature Extraction

Two pre-trained transformers, DINO (Caron et al. 2021) and Point-MAE (Pang et al. 2022) are first applied as deep feature extractors (\mathcal{F}_{RGB} , \mathcal{F}_{PC}) for the contraction of memory bank due to their ability of producing distinct features between normal and anomalous data, following M3DM (Wang et al. 2023b; Heckler, König, and Bergmann 2023). The input data of feature extractors and generated real features are denoted as (I_{RGB}, I_{PC}) and (R_{RGB}, R_{PC}) , respectively.

RGB Feature Extraction. For a given RGB image, $I_{RGB} \in \mathbb{R}^{H \times W \times 3}$, feature extractor \mathcal{F}_{RGB} take it as input and produce a feature map $R_{RGB} \in \mathbb{R}^{H_f \times W_f \times d_1}$. To align feature maps from different modalities, we use up-pooling to obtain new $R_{RGB} \in \mathbb{R}^{2H_f \times 2W_f \times d_1}$. The positional encoding of the feature map is removed.

Point Clouds Feature Extraction and Interpolation. For a given structured point cloud (PC) $I_{PC} \in \mathbb{R}^{H \times W \times 3}$, 3D local shape descriptors (Pang et al. 2022) are created as follows considering the inherent sparsity and disorder properties of point clouds. Farthest point sampling (FPS) (Qi et al. 2017) chooses N points as group center for KNN clustering of M points. Feature extractor \mathcal{F}_{PC} further process N point groups into feature embeddings with dimensions of $N \times d_2$. Then inverse distance weighting (IDW) method (Wang et al. 2023b) is used for the interpolation of obtained features back to each pixel. The down sampled feature map $R_{PC} \in \mathbb{R}^{2H_f \times 2W_f \times d_2}$ is obtained through average pooling.

Cross-Modal Distillation

In order to implement the MTFI pipeline of fewer modalities inference, we build a cross-modal distillation network to generate hallucinations that retain the information of missing modalities. There are four possible distillation routes to satisfy the model: (i) Feature-to-Feature Distillation; (ii) Feature-to-Input Distillation; (iii) Input-to-Feature Distillation; and (iv) Input-to-Input distillation. Since (iv) still needs to extract features for estimation, which is essentially the same as (ii), we only implemented (i-iii) for MTFI as shown in Figure 2. The cross-modal distillation networks are denoted as \mathcal{C}_{F2F} , \mathcal{C}_{F2I} and \mathcal{C}_{I2F} .

Feature-to-Feature (F2F) Distillation. Directly establishing a mapping from feature space to feature space is common and effective (Costanzino et al. 2023; Garcia, Morerio, and Murino 2018; Wang et al. 2023a). Even if the differences between modalities are large, the neural network can still learn common features or estimate new features. For a given feature $R_{PC}^{i,j}$ in a feature map R_{PC} , the estimated hallucination feature $H_{fRGB}^{i,j}$ can be obtained as follows:

$$H_{fRGB}^{i,j} = \mathcal{C}_{F2F}(R_{PC}^{i,j}) \quad (1)$$

By generation of all features, we obtain the predicted feature maps $H_{fRGB}^{i,j}$ of dimensions $2H_f \times 2W_f \times d_1$. The estimation of $H_{PC}^{i,j}$ is similar based on the feature map $R_{fRGB}^{i,j}$.

Feature-to-Input (F2I) Distillation. What type of knowledge can be retained during cross-modal distillation is unknown, so it is valuable to compare results with the feature extractor of missing modality or not. Estimating the input of one modality from the features (inputs) of another modality has been extensively studied as Single Image Depth Estimation (SIDS) or 3D Point Cloud Generation. The hallucination input $H_{iRGB} \in \mathbb{R}^{H \times W \times 3}$ and feature map $H_{fRGB} \in \mathbb{R}^{2H_f \times 2W_f \times d_1}$ are estimated based on the correspond feature map $R_{PC} \in \mathbb{R}^{2H_f \times 2W_f \times d_2}$ as:

$$H_{fRGB} = \mathcal{F}_{RGB}(H_{iRGB}), H_{iRGB} = \mathcal{C}_{F2I}(R_{PC}) \quad (2)$$

Input to Feature (I2F) Distillation. Similarly, it is also feasible to generate features of missing modalities through existing inputs as equation 3, which reduces the limitations of the feature extractor on the hidden layer and is closer to the teacher-student architecture of typical knowledge distillation. All background points in PCs input $I_{PC} \in \mathbb{R}^{H \times W \times 3}$ have been removed. For reverse distillation of H_{fPC} , the corresponding RGB points are also set to 0.

$$H_{fRGB} = \mathcal{C}_{I2F}(I_{PC}) \quad (3)$$

Optimization. During the training, \mathcal{C}_{F2F} , \mathcal{C}_{F2I} or \mathcal{C}_{I2F} are optimized based on all samples from anomaly-free training set by minimizing the average loss of per-pixel’s distance between the real and hallucination. Considering the performance and computational cost, L2 distance is selected as the metric from L1, L2 and cosine distance. (Appendix)

Coreset Selection for Memory Bank Construction

The memory bank method determines the anomaly score by measuring the distance between the sample features to be tested and the normal features in the memory bank. Thus, it is crucial to make the memory bank as comprehensively as possible and remove duplicate features to reduce the calculation cost instead of storing all features as \mathcal{M} for inference. To maximize the representative of the memory bank $\mathcal{M}_{coreset}$, the solution of an NP-Hard problem (Wolsey and Nemhauser 2014) needs to be found:

$$\mathcal{M}_{coreset} = \arg \min_{\mathcal{M}_{coreset} \in \mathcal{M}} \max_{m \in \mathcal{M}} \min_{n \in \mathcal{M}_{coreset}} D_c(m, n) \quad (4)$$

A greedy algorithm for sampling is used similar to Patch-Core (Roth et al. 2022) to address this problem. Starting from a random given patch embedding $p_i \in \mathbb{R}^{1 \times d}$ from a feature set $S \in \mathbb{R}^{P \times d}$ with P patch features, a new selected patch p_{i+1} is calculated as follows:

$$p_{i+1} = \arg \max_{p_j \in S, i \neq j} D_c(p_i, p_j) \quad (5)$$

D_c is the distance metric which needs to be consistent with the one used to calculate the anomaly score in section . The memory banks \mathcal{M}_{PC} , \mathcal{M}_{RGB} in Figure 2 are constructed by adding the selected patch to memory and calculate the new patch through p_{i+1} iteratively for limited times. However, as the number of samples increases, the process of calculating high dimensional distance is still time-consuming. Sparse Random Projection (Wang et al. 2023b; Pedregosa et al. 2011) is applied to reduce the dimension and accelerate computation with acceptable embedding quality.

Decision Layer Fusion

At inference time, the model calculates anomaly scores by comparing each real or generated feature map F_{PC} and F_{RGB} with correspond memory bank. Two One-Class Support Vector Machine using Stochastic Gradient Descent, C_c and C_s , are applied as the decision layer fusion for image classification and segmentation as:

$$c = C_c(\alpha\psi(F_{PC}, \mathcal{M}_{PC}), \beta\psi(F_{RGB}, \mathcal{M}_{RGB})) \quad (6)$$

$$s = C_s(\alpha\phi(F_{PC}, \mathcal{M}_{PC}), \beta\phi(F_{RGB}, \mathcal{M}_{RGB})) \quad (7)$$

Method	Bagel	Cable Gland	Carrot	Cookie	Dowel	Foam	Peach	Potato	Rope	Tire	Mean	
I-AUROC	FPFH(Horwitz and Hoshen 2023)	0.825	0.551	0.952	0.797	0.883	0.582	0.758	0.889	0.929	0.653	0.782
	AST(Rudolph et al. 2023)	0.881	0.576	0.965	0.957	0.679	0.797	0.990	0.915	0.956	0.611	0.833
	M3DM(Wang et al. 2023b)	0.941	0.651	0.965	0.969	0.905	0.760	0.880	0.974	0.926	0.765	0.874
	Shape-guided(Chu et al. 2023)	0.983	0.682	0.978	0.998	0.960	0.737	0.993	0.979	0.966	0.871	0.916
	Ours _{single}	0.973	0.687	0.927	0.965	0.838	0.732	0.857	0.987	0.864	0.863	0.860
	Ours _{F2F}	0.992	0.893	0.977	0.960	0.953	0.883	0.950	0.937	0.943	0.893	0.938
	Ours _{F2I}	0.976	0.780	0.974	0.810	0.879	0.735	0.929	0.877	0.855	0.815	0.863
Ours _{I2F}	0.981	0.719	0.842	0.963	0.965	0.437	0.815	0.816	0.875	0.892	0.820	
AUPRO	FPFH(Horwitz and Hoshen 2023)	0.973	0.879	0.982	0.906	0.892	0.735	0.977	0.982	0.956	0.961	0.924
	M3DM(Wang et al. 2023b)	0.943	0.818	0.977	0.882	0.881	0.743	0.958	0.974	0.950	0.929	0.906
	Shape-guided(Chu et al. 2023)	0.974	0.871	0.981	0.924	0.898	0.773	0.978	0.983	0.955	0.969	0.931
	Ours _{single}	0.947	0.826	0.977	0.882	0.881	0.767	0.967	0.978	0.947	0.940	0.911
	Ours _{F2F}	0.968	0.907	0.982	0.933	0.918	0.726	0.982	0.983	0.969	0.974	0.934
	Ours _{F2I}	0.963	0.826	0.978	0.879	0.947	0.709	0.972	0.965	0.951	0.940	0.912
	Ours _{I2F}	0.947	0.973	0.973	0.893	0.935	0.843	0.970	0.956	0.964	0.968	0.942

Table 1: I-AUROC and AUPRO results on MVTec 3D-AD for 3D based methods.

c and s are final predication score of image classification and pixel segmentation. In order to balance the mean of anomaly scores between modalities, correction factor α and β are introduced. ψ and ϕ are anomaly scores of classification and segmentation from (Roth et al. 2022) formulated as:

$$\psi(F, \mathcal{M}) = D_d(F^{(i,j),*}, m^*) \quad (8)$$

$$\phi(F, \mathcal{M}) = \left\{ \min_{m \in \mathcal{M}} D_d(F^{i,j}, m), \text{ for } F^{i,j} \in F \right\} \quad (9)$$

D_d is the distance metric. The anomaly score of a image is determined by the maximum distance of between a feature and its most similar feature m in memory bank:

$$F^{(i,j),*}, m^* = \arg \max_{F^{(i,j)} \in F} \arg \min_{m \in \mathcal{M}} D_d(F^{i,j}, m) \quad (10)$$

Experiments

Experimental Setup

Dataset and Evaluation Metrics. Majority of recent studies in multimodal IAD research are on the MVTec 3D-AD (Bergmann. et al. 2022) dataset, which includes aligned PCs and RGB images of real-world objects. This dataset consists of 10 classes of objects and each class may have 3-5 types of defects with pixel-level ground truth. Objects were recorded with an structured light 3D sensor. Every sample contains one image with (x, y, z) values of corresponding PCs and another image with (r, g, b) values. We also evaluate our methods on Eyecandies (Bonfiglioli et al. 2022), a pure synthetic RGB+3D IAD dataset. The image and pixel level anomaly detection performance are evaluated with Area Under the Receiver Operator Curve (I-AUROC and P-AUROC) and Area Under the Per-Region Overlap (AUPRO) following (Wang et al. 2023b; Bergmann. et al. 2022). AUPRO is the average overlap of the prediction with each connected component of ground truth which reduces the impact of the size of anomalies compared with P-AUROC.

Data Pre-processing. To solve the classification errors caused by background artifacts, the background plane of PCs was estimated based on the RANSAC (Fischler and Bolles 1981) method following (Wang et al. 2023b) and (Horwitz and Hoshen 2023). Then we replaced the values of points within 0.005 from the plane with zeros.

Implementation Details. Two feature extractors DINO (Caron et al. 2021) and Point-MAE (Pang et al. 2022) pre-trained on ImageNet (Deng et al. 2009) and ShapeNet (Chang et al. 2015) are used as (Wang et al. 2023b). For an input RGB image, (224, 224, 3), the corresponding feature map is up-sampled to (56×56, 768). For the PCs, FPS is first used to convert it into 1024 groups and each group has 128 points (1024, 384) as the input of point transformer. The features generated by the point transformer are interpolated into a (56×56, 768) feature map through the inverse distance weight method, yielding aligned RGB and PCs feature maps. The learning rate of One-Class Support Vector Machine using Stochastic Gradient Descent for decision layer fusion is set as 1×10^{-4} for 1000 steps.

For three levels of cross-modal distillation, three different networks are employed to provide suitable fitting capabilities in accordance with previous studies. For F2F distillation, a three-layer MLP with (1920, 1920, 768) units is used to generate the hallucination of cross-modal feature. For I2F distillation, we adopted the high-resolution branch of HRNet (Wang et al. 2020a) to retain more information and generate high-resolution feature maps. A convolutional network similar to the depth estimation head of DINOv2 (Oquab et al. 2023) was used for F2I distillation. Adam optimizer was applied with a batch size of 32 and 10 epochs warm-up to train all three types of networks for 100 epochs. We report the best results of F2F and F2I distillation setting the learning rate as 0.0005 at 64/39 (PCs) and 49/54 (RGB) epochs respectively. For I2F distillation, we reduce the learning rate to 0.0003 to avoid divergence and obtain the optimal results from 24 epochs for PCs and 34 epochs for RGB images. The best epochs are selected by performing inference on the validation set with trained distillation network.

Method	Bagel	Cable Gland	Carrot	Cookie	Dowel	Foam	Peach	Potato	Rope	Tire	Mean	
I-AUROC	PADiM(Defard et al. 2021)	0.975	0.775	0.698	0.582	0.959	0.663	0.858	0.535	0.832	0.760	0.764
	PatchCore(Roth et al. 2022)	0.876	0.880	0.791	0.682	0.912	0.701	0.695	0.618	0.841	0.702	0.770
	CS-Flow(Shi et al. 2022)	0.941	0.930	0.827	0.795	0.990	0.886	0.731	0.471	0.986	0.745	0.830
	AST(Rudolph et al. 2023)	0.947	0.928	0.851	0.825	0.981	0.951	0.895	0.613	0.992	0.821	0.880
	M3DM(Wang et al. 2023b)	0.944	0.918	0.896	0.749	0.959	0.767	0.919	0.648	0.938	0.767	0.850
	Shape-guided(Chu et al. 2023)	0.911	0.936	0.883	0.662	0.974	0.772	0.785	0.641	0.884	0.706	0.815
	Ours _{single}	0.942	0.918	0.896	0.749	0.959	0.767	0.919	0.648	0.941	0.768	0.851
	Ours _{F2F}	0.945	0.926	0.896	0.700	0.965	0.836	0.925	0.644	0.942	0.777	0.856
	Ours _{F2I}	0.918	0.900	0.859	0.750	0.933	0.781	0.832	0.574	0.934	0.744	0.823
	Ours _{I2F}	0.938	0.929	0.897	0.760	0.959	0.802	0.932	0.638	0.941	0.787	0.858
AUPRO	CS-Flow(Shi et al. 2022)	0.855	0.919	0.958	0.867	0.969	0.500	0.889	0.935	0.904	0.919	0.871
	PatchCore(Roth et al. 2022)	0.901	0.949	0.928	0.877	0.892	0.563	0.904	0.932	0.908	0.906	0.876
	PADiM(Defard et al. 2021)	0.980	0.944	0.945	0.925	0.961	0.792	0.966	0.940	0.937	0.912	0.930
	M3DM(Wang et al. 2023b)	0.952	0.972	0.973	0.891	0.932	0.843	0.970	0.956	0.968	0.966	0.942
	Shape-guided(Chu et al. 2023)	0.946	0.972	0.960	0.914	0.958	0.776	0.937	0.949	0.956	0.957	0.933
	Ours _{single}	0.951	0.972	0.973	0.891	0.932	0.843	0.970	0.956	0.968	0.966	0.942
	Ours _{F2F}	0.943	0.971	0.973	0.879	0.936	0.845	0.968	0.956	0.968	0.965	0.940
	Ours _{F2I}	0.897	0.946	0.923	0.842	0.753	0.805	0.927	0.880	0.917	0.930	0.882
	Ours _{I2F}	0.950	0.972	0.973	0.893	0.932	0.849	0.970	0.956	0.968	0.968	0.943

Table 2: I-AUROC and AUPRO results on MVTec 3D-AD for RGB based methods.

Results of MTFI Pipeline (Inference with PCs)

Table 1 shows the I-AUROC and AUPRO of our method and previous work for detecting anomalies on the 10 classes of MVTec 3D-AD and the averages. The P-AUROC is also attached in Appendix. We compared F2F, F2I and I2F of our MTFI pipeline with single memory bank and other methods based on pure PCs or depth images. Both F2F and F2I are substantially better than single memory bank method (F2F: I-AUROC 7.8% \uparrow , AUPRO 2.3% \uparrow ; F2I: I-AUROC 0.3 % \uparrow , AUPRO 0.1 % \uparrow). The highest I-AUROC result is from our MTFI pipeline (F2F, I-AUROC 0.938, AUPRO 0.934), which outperforms the SOTA work, Shape-guided (Chu et al. 2023) with specially designed memory bank for PCs by 2.2 % and 0.3 % for I-AUROC and AUPRO, respectively. This demonstrates the feasibility of cross-modal distillation and the MTFI pipeline for IAD. F2F distillation also has the same performance in image classification as dual RGB+PCs memory banks method, and has faster inference speed (Appendix).

Results of MTFI Pipeline (Inference with RGB)

Exceedingly different results were obtained from MTFI Pipeline (Inference with RGB only) and shown in Table 2. Only slight improvement in F2F and I2F compared can be observed with single RGB memory bank. This asymmetry result indicates that the generated PCs hallucination cannot provide enough information to distinguish between normal and abnormal patches for decision layer fusion.

Ablation Study

We conduct an ablation study to verify the effectiveness of MTFI pipeline and assess the generalizability of asymmetric performance by changing the feature extractor and dataset. We replace the used RGB feature extractor DINO ViT-B/8

Feature Extractors	Single PCs	MTFI PCs	Single RGB	MTFI RGB	Dual RGB+PCs
RGB#1+PCs#1	0.860	0.938	0.851	0.856	0.938
	0.911	0.934	0.942	0.940	0.962
RGB#2+PCs#1	0.860	0.899	0.817	0.817	0.908
	0.911	0.931	0.937	0.938	0.911
RGB#3+PCs#1	0.860	0.884	0.663	0.670	0.873
	0.911	0.920	0.837	0.838	0.911
RGB#1+PCs#2	0.790	0.864	0.851	0.860	0.833
	0.869	0.926	0.942	0.943	0.948
RGB#1+PCs#1 (Eyecandies)	0.732	0.764	0.869	0.874	0.859
	0.684	0.726	0.884	0.884	0.881

Table 3: Ablation study for different feature extractors on MVTec 3D-AD and replacing dataset with Eyecandies. The top and bottom of each row are the average I-AUROC and AUPRO. RGB#1: DINO ViT-B/8, RGB#2: DINO ViT-S/8, RGB#3: ViT-B/8-in21k, PCs#1: Point-MAE, PCs#2: Point-Bert. RGB#1 and PCs#1 are used in previous MTFI study.

with ViT-B/8-in21k and DINO ViT-S/8, PCs feature extractor Point-MAE with Point-Bert, and dataset MVTec 3D-AD with Eyecandies respectively (Table 3). The results based on the MTFI pipeline (inference with PCs) are markedly superior to those based on single PCs memory bank, and even better than dual RGB+PCs memory banks in some cases. But the MTFI pipeline (inference with RGB) is barely an improvement over single RGB memory bank. All those results further demonstrate that MTFI pipeline (inference with PCs) can enhance the utilization of multimodal training data.

Visualization and Analysis of Classification Results of MTFI Pipeline

To provide an intuitive understanding of the differences in detection results, we visualized and manually inspected the

inputs and predictions. The Cable Gland class was investigated first for the dramatically enhanced performance which is mainly attributed to the reduction of false positives and correct identification of ‘thread’ anomalies like Figure 1a. ‘Thread’ class has smaller local shape changes in PCs compared to the other classes ‘bent’, ‘cut’ and ‘hole’ where large chunks of structure are obviously bent or missing (Figure 3 and Appendix). In conventional RGB feature extraction, color and texture are generally accepted to be the most effective features for classification (Horwitz and Hoshen 2023; Mohanaiah, Sathyanarayana, and GuruKumar 2013) and geometry texture information can also be extracted from PCs (Jang et al. 2013; Freitas, Diniz, and Farias 2023) through changes in local shape. For ‘thread’, local texture disappears due to damage, which is vaguely visible in the PCs and is confused by the model as a normal feature. But the texture of this region is quite different from the of normal area in the RGB image. For cross-modal KD, the RGB hallucination generated through PCs preserve this texture abnormality and provide discrimination. This is evidenced by the improved classification of ‘crack’ in Cookie class and ‘contamination’ in Foam class. There are many pits on the cookie surface that the PCs model considers to be similar to cracks (Figure 1b) and the undulating structure of the foam surface is indistinguishable from the contamination (Figure 1c). This limited local shape difference cannot provide specific abnormal information, but the generated RGB hallucination is obviously different from the normal area. In short, the MTFI pipeline enables features that are visible in both modalities but insufficient for accurate discrimination in the original modality to be accurately classified, potentially through mapping shared or similar information among modalities like texture.

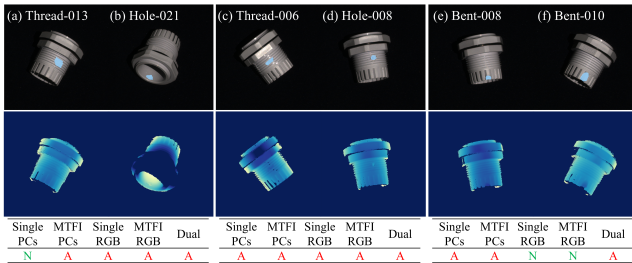


Figure 3: Visualization of 6 representative abnormal samples with image classification results (A: Abnormal, N: Normal). (a, b) require cross-modal distillation to aid classification due to small shape changes. (c, d) can be directly classified by single PCs bank due to obvious shape changes. (e, f) can only be correctly classified in the PCs based method, although the structure changes obviously, the anomalies are too similar to other structures in the RGB image.

Analysis of Asymmetry Results of Cross-Modal Distillation

However, the results of MTFI pipeline (inference with RGB) reveal that anomalies visible in both modalities is only one sufficient condition. Comparing MTFI pipeline with PCs and RGB images from Cable Grand class as an example,

anomalies that cannot be accurately classified using RGB images are mainly from the ‘bent’ anomaly, *e.g.*, Bent-8 and Bent-10 in Figure 3e, f. This bending of part of the structure is very similar to other structures in RGB images. It needs to be classified through spatial information (shape features), which is what PCs are better at. Previous research has proven that it is challenging to extract shape or spatial features from a single RGB image, especially with limited data (Koch et al. 2018; Niu, Li, and Xu 2018). We speculate that the asymmetry results due to the insufficient spatial information in RGB modality, which is necessary for accurate PC hallucination generation to distinguish normal and abnormal inputs. This is also mirrored in almost the same ranking of sample anomaly score from MTFI pipeline (inference with RGB) and single RGB memory bank. Results of ‘hole’ and ‘combined’ from Cookie class and ‘cut’ from Foam class are consistent with the assumption of lacking spatial information (Appendix). In summary, two points should be noted to enhance single-modal inference through MTFI pipeline: 1) anomalies must be visible in both modalities but can be insignificant in one modality for classification. 2) shared information like texture or spatial information needs to be both present and represented in latent space to help generate hallucination with abnormality. Although complex representations are challenging for humans to comprehend and, the inability to generate valuable PCs hallucination using RGB that lacks spatial information highlights the significance of shared information.

Conclusion

In this work, we have developed a effective framework based on MTFI pipeline driven via cross-modality distillation for multimodal IAD. It can retain partial information of the missing modality by generating its hallucination during inference. The MTFI pipeline (inference with PCs) delivers significantly better results compared with single PCs memory bank, but the MTFI pipeline (inference with RGB) only has a moderate positive effect. By manually inspecting the variation in classification results, we attribute this to the inability of generating PCs hallucination with abnormality from RGB for lacking of spatial information. For anomalies that are confused by the single PCs memory bank due to limited shape changes in the 3D structure, the RGB hallucination generated through modal shared information like texture provides effective discrimination.

Limitations

Although IAD methods based on pre-trained feature extractors have shown unusual performance, this dependence hinders the introduction of new modalities without large datasets. Further development of reconstruction-based IAD methods and transfer learning may address this issue. In addition, we have demonstrated the good results of CMDIAD based on the MTFI pipeline on two datasets and multiple feature extractors, but its application in real scenarios still requires a large amount of high-quality in-line and near-line data, which is also our subsequent priority work.

Appendix

Additional Experiment Results on MVTec 3D-AD

The experimental data not included in the main text are attached here, P-AUROC results on MVTec 3D-AD (Table A1) and I-AUROC and AUPRO results on MVTec 3D-AD for RGB+PCs based methods (Table A2). Although many studies still report P-AUROC, the comparative value is low because the values are very high and close. In order to compare the efficiency of utilizing multimodal data, we also tested the basic dual memory bank method shown in Table A2. The experimental results on the distance metrics (L1, L2, Cosine) are shown in Table A3.

Visualization of Anomalies of Cable Gland Class

As illustrated in Figure A1, among the four types of anomalies of the Cable Gland class, ‘thread’ anomaly has the smallest change of shape and interference from thread.



Figure A1: Visualization of ‘bent’, ‘cut’, ‘hole’ and ‘thread’ anomalies of Cable Gland class.

Supplementary Prediction Results of Samples in Figure 3

The prediction results of the six samples in Figure 3 are shown in Figures A2-A7 as a supplement.

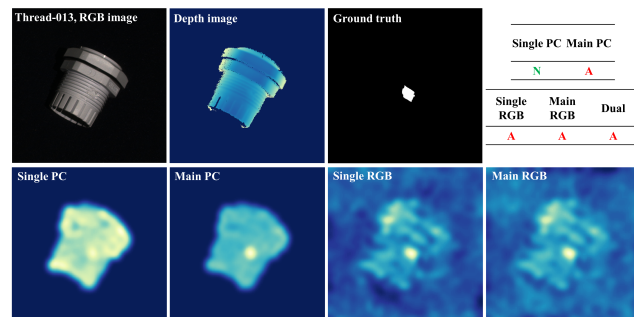


Figure A2: Visualization and Prediction Results of Cable Gland-Test-Thread-013. (A: Abnormal, N: Normal)

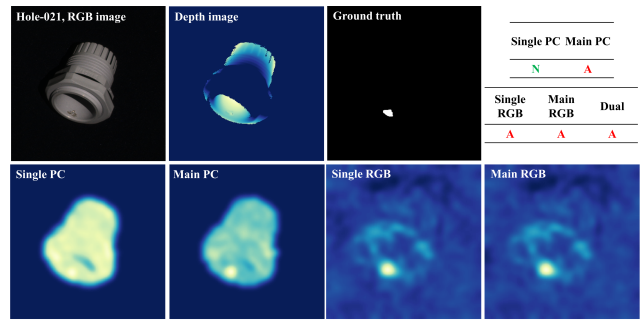


Figure A3: Visualization and Prediction Results of Cable Gland-Test-Hole-021. (A: Abnormal, N: Normal)

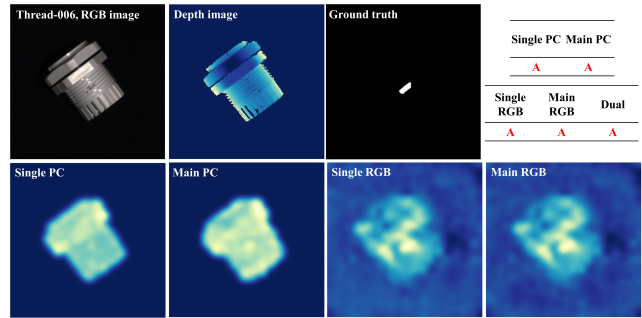


Figure A4: Visualization and Prediction Results of Cable Gland-Test-Thread-006. (A: Abnormal, N: Normal)

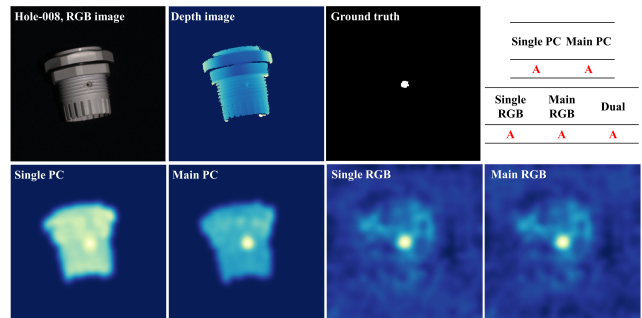


Figure A5: Visualization and Prediction Results of Cable Gland-Test-Hole-008. (A: Abnormal, N: Normal)

Prediction Results of ‘hole’ and ‘combined’ anomalies from Cookie class

Prediction Results of ‘hole’ (A8) and ‘combined’ (A9) anomalies from Cookie class are also visualized here to support ideas in Section Analysis of Asymmetry Results of Cross-Modal Distillation.

Experiments Compute Resources

We conducted experiments on a single NVIDIA RTX A6000 with Linux driver 535.54.03. The CPU is INTEL W5-2455X with 256 G DRR5 memory. For single memory bank method, it needs about 50 and 70 minutes and maximum 50 GB memory for RGB and PCs, respectively. For training the

Method	Bagel	Cable Gland	Carrot	Cookie	Dowel	Foam	Peach	Potato	Rope	Tire	Mean	
3D	FPFH(Chu et al. 2023)	0.994	0.966	0.999	0.946	0.966	0.927	0.996	0.999	0.996	0.99	0.978
	M3DM(Wang et al. 2023b)	0.981	0.949	0.997	0.932	0.959	0.925	0.989	0.995	0.994	0.981	0.97
	Ours _{single}	0.983	0.95	0.997	0.932	0.959	0.94	0.991	0.996	0.994	0.984	0.973
	Ours _{FtoF}	0.992	0.975	0.999	0.96	0.975	0.924	0.998	0.998	0.998	0.996	0.981
RGB	PatchCore(Roth et al. 2022)	0.983	0.984	0.98	0.974	0.972	0.849	0.976	0.983	0.987	0.977	0.967
	M3DM(Wang et al. 2023b)	0.992	0.99	0.994	0.977	0.983	0.955	0.994	0.99	0.995	0.994	0.987
	Ours _{single}	0.992	0.993	0.994	0.977	0.983	0.956	0.993	0.99	0.995	0.994	0.987
	Ours _{FtoF}	0.992	0.993	0.994	0.976	0.983	0.956	0.993	0.99	0.995	0.994	0.987
RGB+3D	AST(Rudolph et al. 2023)	-	-	-	-	-	-	-	-	-	-	0.976
	PatchCore(Roth et al. 2022)	0.996	0.992	0.997	0.994	0.981	0.974	0.996	0.998	0.994	0.995	0.992
	M3DM(Wang et al. 2023b)	0.995	0.993	0.997	0.985	0.985	0.984	0.996	0.994	0.997	0.996	0.992
	Ours _{dual}	0.995	0.993	0.996	0.976	0.984	0.988	0.996	0.995	0.997	0.996	0.992

Table A1: P-AUROC results on MVTec 3D-AD.

Method	Bagel	Cable Gland	Carrot	Cookie	Dowel	Foam	Peach	Potato	Rope	Tire	Mean	
I-AUROC	3D-ST(Bergmann and Sattlegger 2023)	0.950	0.483	0.986	0.921	0.905	0.632	0.945	0.988	0.976	0.542	0.833
	PatchCore+FPFH(Horwitz and Hoshen 2023)	0.918	0.748	0.967	0.883	0.932	0.582	0.896	0.912	0.921	0.886	0.865
	AST(Rudolph et al. 2023)	0.983	0.873	0.976	0.971	0.932	0.885	0.974	0.981	1.000	0.797	0.937
	M3DM(Wang et al. 2023b)	0.994	0.909	0.972	0.976	0.960	0.942	0.973	0.899	0.972	0.850	0.945
	Shape-guided(Chu et al. 2023)	0.986	0.894	0.983	0.991	0.976	0.857	0.990	0.965	0.960	0.869	0.947
	Ours	0.992	0.893	0.977	0.960	0.953	0.883	0.950	0.937	0.943	0.893	0.938
AUPRO	3D-ST(Bergmann and Sattlegger 2023)	0.950	0.483	0.986	0.921	0.905	0.632	0.945	0.988	0.976	0.542	0.833
	PatchCore+FPFH(Horwitz and Hoshen 2023)	0.976	0.969	0.979	0.973	0.933	0.888	0.975	0.981	0.950	0.971	0.959
	M3DM(Wang et al. 2023b)	0.970	0.971	0.979	0.950	0.941	0.932	0.977	0.971	0.971	0.975	0.964
	Shape-guided(Chu et al. 2023)	0.981	0.973	0.982	0.971	0.962	0.978	0.981	0.983	0.974	0.975	0.976
	Ours	0.970	0.971	0.977	0.932	0.934	0.946	0.978	0.970	0.970	0.974	0.962

Table A2: I-AUROC and AUPRO results on MVTec 3D-AD for RGB+PCs based methods.

	Method	Bagel	Cable Gland	Carrot	Cookie	Dowel	Foam	Peach	Potato	Rope	Tire	Mean
I-AUROC	L2	0.992	0.893	0.977	0.960	0.953	0.883	0.950	0.937	0.943	0.893	0.938
	L1	0.986	0.823	0.994	0.987	0.960	0.786	0.992	0.865	0.947	0.944	0.928
	Cosine	0.994	0.795	0.993	0.983	0.932	0.754	0.995	0.894	0.921	0.953	0.921
P-AUROC	L2	0.992	0.975	0.999	0.960	0.975	0.924	0.998	0.998	0.998	0.996	0.981
	L1	0.992	0.972	0.999	0.960	0.975	0.927	0.997	0.998	0.997	0.995	0.981
	Cosine	0.993	0.973	0.998	0.977	0.982	0.915	0.998	0.998	0.997	0.996	0.983
AUPRO	L2	0.968	0.907	0.982	0.933	0.918	0.726	0.982	0.983	0.969	0.974	0.934
	L1	0.968	0.897	0.982	0.931	0.917	0.727	0.981	0.982	0.968	0.971	0.932
	Cosine	0.972	0.900	0.981	0.956	0.940	0.694	0.982	0.983	0.972	0.973	0.935

Table A3: I-AUROC and AUPRO results based on MTFI pipeline (FtoF, PCs as main modality) with Different Distance Metrics.

distillation network, it takes about 30 s to 1 min per epoch (TF32 is used). Since the step of transferring tensors to GPU memory in PyTorch is time-consuming, we loaded the data into GPU memory in advance to speed up the calculation. Running the MTFI pipeline with the trained distillation network takes approximately two hours. Unfortunately, training the distillation network is an intermediate step, and lower loss does not bring the best results to the MTFI pipeline. We need to run the MTFI pipeline multiple times with different

checkpoints to find the optimized point. This also means that the general way of calculating per-pixel distance may need to be improved. For single memory bank and dual memory bank methods, you only need to run it once to get a result of test set defect inspection. For the two-stage MTFI pipeline, the cross-modal KD network needs to be trained first and then inference needs to be performed (i.e., it needs to be run twice). Choosing the appropriate number of epochs for training the cross-modal KD network requires repeatedly running

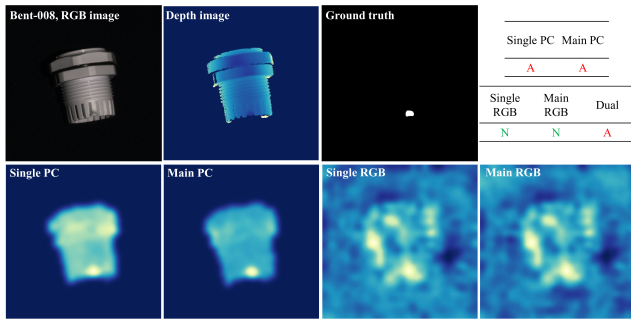


Figure A6: Visualization and Prediction Results of Cable Gland-Test-Bent-008. (A: Abnormal, N: Normal)

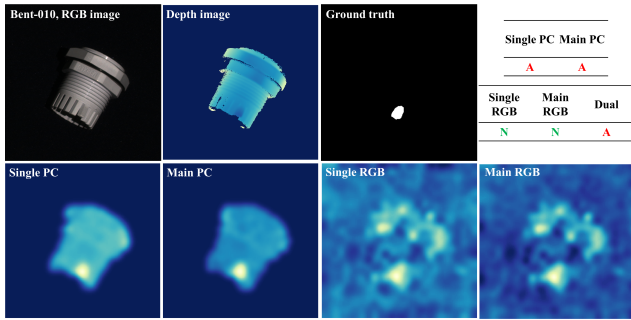


Figure A7: Visualization and Prediction Results of Cable Gland-Test-Bent-010. (A: Abnormal, N: Normal)

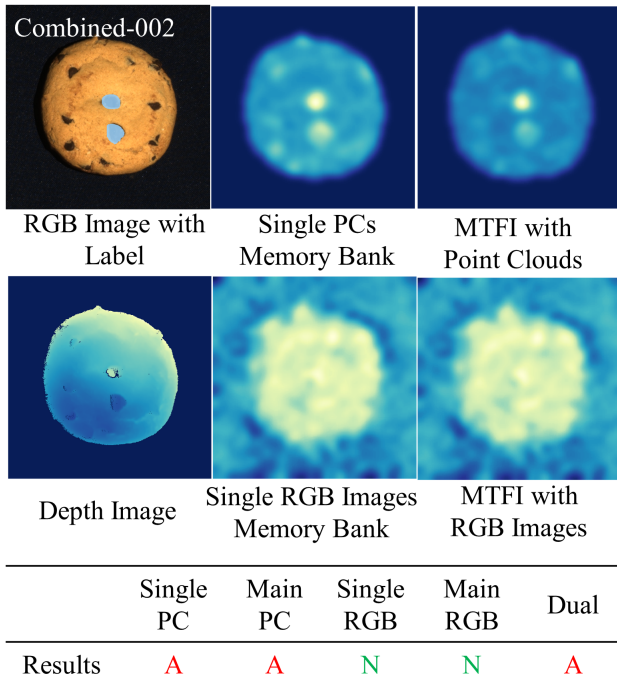
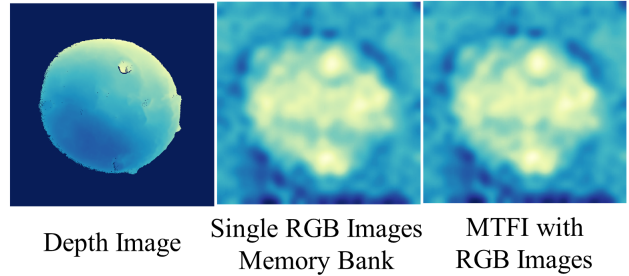
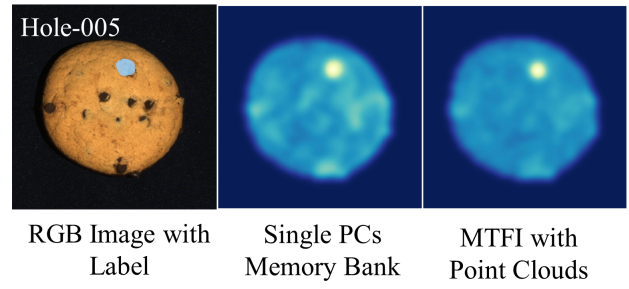


Figure A8: Visualization and Prediction Results of 'hole' anomalies from Cookie class. (A: Abnormal, N: Normal)



	Single PC	Main PC	Single RGB	Main RGB	Dual
Results	A	A	N	N	A

Figure A9: Visualization and Prediction Results of 'combined' anomalies from Cookie class. (A: Abnormal, N: Normal)

the second stage using a grid search, and we searched in units of 5 epochs.

Inference Speed

We also measured inference speed of our MTFI pipeline (F2F, Inference with PCs) with similar methods. It can be seen that the inference time is basically in line with the expectations of the network structure. Due to the absence of feature fusion network and the omission of RGB feature extraction network, our method is slightly faster than M3DM. Although Crossmodal feature mapping also uses the memory bank method, it is significantly faster. This is partly due to network improvements, but more because some CPU calculations are transferred to the GPU.

Method	Inference Time(s)
BTF (Horwitz and Hoshen 2023)	2.19
Shape-guided (Chu et al. 2023)	2.05
M3DM (Wang et al. 2023b)	1.95
Crossmodal feature mapping (Costanzino et al. 2023)	0.14
Ours	
(Dual RGB+PCs memory bank)	1.90
Ours	
(MTFI, F2F, Inference with PCs only)	1.74

References

- Bergmann, P.; Jin, X.; Sattlegger, D.; and Steger, C. 2022. The MVTEC 3D-AD Dataset for Unsupervised 3D Anomaly Detection and Localization. In *Proceedings of the 17th International Joint Conference on Computer Vision, Imaging and Computer Graphics Theory and Applications (VISIGRAPP 2022) - Volume 5: VISAPP*, 202–213. INSTICC, SciTePress. ISBN 978-989-758-555-5.
- Bergmann, P.; Löwe, S.; Fauser, M.; Sattlegger, D.; and Steger, C. 2018. Improving unsupervised defect segmentation by applying structural similarity to autoencoders. *arXiv preprint arXiv:1807.02011*.
- Bergmann, P.; and Sattlegger, D. 2023. Anomaly Detection in 3D Point Clouds Using Deep Geometric Descriptors. In *Proceedings of the IEEE/CVF Winter Conference on Applications of Computer Vision (WACV)*, 2613–2623.
- Bonfiglioli, L.; Toschi, M.; Silvestri, D.; Fioraio, N.; and De Gregorio, D. 2022. The Eyecandies Dataset for Unsupervised Multimodal Anomaly Detection and Localization. In *Proceedings of the Asian Conference on Computer Vision (ACCV)*, 3586–3602.
- Cao, K.; Xia, Y.; Yao, J.; Han, X.; Lambert, L.; Zhang, T.; Tang, W.; Jin, G.; Jiang, H.; Fang, X.; et al. 2023. Large-scale pancreatic cancer detection via non-contrast CT and deep learning. *Nature medicine*, 29(12): 3033–3043.
- Caron, M.; Touvron, H.; Misra, I.; Jégou, H.; Mairal, J.; Bojanowski, P.; and Joulin, A. 2021. Emerging properties in self-supervised vision transformers. In *Proceedings of the IEEE/CVF international conference on computer vision*, 9650–9660.
- Chang, A. X.; Funkhouser, T.; Guibas, L.; Hanrahan, P.; Huang, Q.; Li, Z.; Savarese, S.; Savva, M.; Song, S.; Su, H.; et al. 2015. Shapenet: An information-rich 3d model repository. *arXiv preprint arXiv:1512.03012*.
- Chu, Y.-M.; Liu, C.; Hsieh, T.-I.; Chen, H.-T.; and Liu, T.-L. 2023. Shape-Guided Dual-Memory Learning for 3D Anomaly Detection. In *Proceedings of the 40th International Conference on Machine Learning*, 6185–6194.
- Costanzino, A.; Ramirez, P. Z.; Lisanti, G.; and Di Stefano, L. 2023. Multimodal Industrial Anomaly Detection by Crossmodal Feature Mapping. *arXiv preprint arXiv:2312.04521*.
- de Haan, P.; and Löwe, S. 2021. Contrastive predictive coding for anomaly detection. *arXiv preprint arXiv:2107.07820*.
- Defard, T.; Setkov, A.; Loesch, A.; and Audigier, R. 2021. Padim: a patch distribution modeling framework for anomaly detection and localization. In *International Conference on Pattern Recognition*, 475–489. Springer.
- Deng, J.; Dong, W.; Socher, R.; Li, L.-J.; Li, K.; and Fei-Fei, L. 2009. ImageNet: A large-scale hierarchical image database. In *2009 IEEE Conference on Computer Vision and Pattern Recognition*, 248–255.
- Fischler, M. A.; and Bolles, R. C. 1981. Random sample consensus: a paradigm for model fitting with applications to image analysis and automated cartography. *Communications of the ACM*, 24(6): 381–395.
- Freitas, X. G.; Diniz, R.; and Farias, M. C. 2023. Point cloud quality assessment: unifying projection, geometry, and texture similarity. *The Visual Computer*, 39(5): 1907–1914.
- Fu, Y.; and Yao, X. 2022. A review on manufacturing defects and their detection of fiber reinforced resin matrix composites. *Composites Part C: Open Access*, 8: 100276.
- Garcia, N. C.; Morerio, P.; and Murino, V. 2018. Modality distillation with multiple stream networks for action recognition. In *Proceedings of the European Conference on Computer Vision (ECCV)*, 103–118.
- Heckler, L.; König, R.; and Bergmann, P. 2023. Exploring the importance of pretrained feature extractors for unsupervised anomaly detection and localization. In *Proceedings of the IEEE/CVF Conference on Computer Vision and Pattern Recognition*, 2916–2925.
- Horwitz, E.; and Hoshen, Y. 2023. Back to the feature: classical 3d features are (almost) all you need for 3d anomaly detection. In *Proceedings of the IEEE/CVF Conference on Computer Vision and Pattern Recognition*, 2967–2976.
- Jang, G.-R.; Shin, Y.-D.; Yoon, J.-S.; Park, J.-H.; Bae, J.-H.; Lee, Y.-S.; and Baeg, M.-H. 2013. Real-time polygon generation and texture mapping for tele-operation using 3D point cloud data. *Journal of institute of Control, Robotics and systems*, 19(10): 928–935.
- Kim, Y.; Jang, H.; Lee, D.; and Choi, H.-J. 2022. Altub: Alternating training method to update base distribution of normalizing flow for anomaly detection. *arXiv preprint arXiv:2210.14913*.
- Koch, T.; Liebel, L.; Fraundorfer, F.; and Korner, M. 2018. Evaluation of cnn-based single-image depth estimation methods. In *Proceedings of the European Conference on Computer Vision (ECCV) Workshops*, 0–0.
- Lee, S.; Lee, S.; and Song, B. C. 2022. Cfa: Coupled-hypersphere-based feature adaptation for target-oriented anomaly localization. *IEEE Access*, 10: 78446–78454.
- Liang, Y.; Zhang, J.; Zhao, S.; Wu, R.; Liu, Y.; and Pan, S. 2023. Omni-frequency channel-selection representations for unsupervised anomaly detection. *IEEE Transactions on Image Processing*.
- Liu, J.; Xie, G.; Wang, J.; Li, S.; Wang, C.; Zheng, F.; and Jin, Y. 2024. Deep industrial image anomaly detection: A survey. *Machine Intelligence Research*, 21(1): 104–135.
- Mohanaiah, P.; Sathyanarayana, P.; and GuruKumar, L. 2013. Image texture feature extraction using GLCM approach. *International journal of scientific and research publications*, 3(5): 1–5.
- Niu, C.; Li, J.; and Xu, K. 2018. Im2struct: Recovering 3d shape structure from a single rgb image. In *Proceedings of the IEEE conference on computer vision and pattern recognition*, 4521–4529.
- Oquab, M.; Darcet, T.; Moutakanni, T.; Vo, H.; Szafraniec, M.; Khalidov, V.; Fernandez, P.; Haziza, D.; Massa, F.; El-Nouby, A.; et al. 2023. Dinov2: Learning robust visual features without supervision. *arXiv preprint arXiv:2304.07193*.

- Pang, Y.; Wang, W.; Tay, F. E.; Liu, W.; Tian, Y.; and Yuan, L. 2022. Masked autoencoders for point cloud self-supervised learning. In *European conference on computer vision*, 604–621. Springer.
- Pedregosa, F.; Varoquaux, G.; Gramfort, A.; Michel, V.; Thirion, B.; Grisel, O.; Blondel, M.; Prettenhofer, P.; Weiss, R.; Dubourg, V.; Vanderplas, J.; Passos, A.; Cournapeau, D.; Brucher, M.; Perrot, M.; and Duchesnay, E. 2011. Scikit-learn: Machine Learning in Python. *Journal of Machine Learning Research*, 12: 2825–2830.
- Qi, C. R.; Yi, L.; Su, H.; and Guibas, L. J. 2017. Pointnet++: Deep hierarchical feature learning on point sets in a metric space. *Advances in neural information processing systems*, 30.
- Qian, S.; Xu, J.; Liu, Z.; Ma, L.; and Gao, S. 2022. UNIF: United neural implicit functions for clothed human reconstruction and animation. In *European Conference on Computer Vision*, 121–137. Springer.
- Reynolds, C. D.; Slater, P. R.; Hare, S. D.; Simmons, M. J.; and Kendrick, E. 2021. A review of metrology in lithium-ion electrode coating processes. *Materials & Design*, 209: 109971.
- Roth, K.; Pemula, L.; Zepeda, J.; Schölkopf, B.; Brox, T.; and Gehler, P. 2022. Towards total recall in industrial anomaly detection. In *Proceedings of the IEEE/CVF Conference on Computer Vision and Pattern Recognition*, 14318–14328.
- Rudolph, M.; Wehrbein, T.; Rosenhahn, B.; and Wandt, B. 2023. Asymmetric student-teacher networks for industrial anomaly detection. In *Proceedings of the IEEE/CVF winter conference on applications of computer vision*, 2592–2602.
- Salehi, M.; Sadjadi, N.; Baselizadeh, S.; Rohban, M. H.; and Rabiee, H. R. 2021. Multiresolution knowledge distillation for anomaly detection. In *Proceedings of the IEEE/CVF conference on computer vision and pattern recognition*, 14902–14912.
- Shi, H.; Zhou, Y.; Yang, K.; Yin, X.; and Wang, K. 2022. CSFlow: Learning optical flow via cross strip correlation for autonomous driving. In *2022 IEEE intelligent vehicles symposium (IV)*, 1851–1858. IEEE.
- Sun, M.; Zhang, X.; Ma, J.; Xie, S.; Liu, Y.; and Yu, P. S. 2023. Inconsistent Matters: A Knowledge-Guided Dual-Consistency Network for Multi-Modal Rumor Detection. *IEEE Transactions on Knowledge and Data Engineering*, 35(12): 12736–12749.
- Tailanian, M.; Musé, P.; and Pardo, Á. 2021. A multi-scale a contrario method for unsupervised image anomaly detection. In *2021 20th IEEE International Conference on Machine Learning and Applications (ICMLA)*, 179–184. IEEE.
- Tao, X.; Gong, X.; Zhang, X.; Yan, S.; and Adak, C. 2022. Deep learning for unsupervised anomaly localization in industrial images: A survey. *IEEE Transactions on Instrumentation and Measurement*, 71: 1–21.
- Teng, Y.; Li, H.; Cai, F.; Shao, M.; and Xia, S. 2022. Unsupervised visual defect detection with score-based generative model. *arXiv preprint arXiv:2211.16092*.
- Vapnik, V. 2006. *Estimation of dependences based on empirical data*. Springer Science & Business Media.
- Vapnik, V.; and Vashist, A. 2009a. A new learning paradigm: Learning using privileged information. *Neural networks*, 22(5-6): 544–557.
- Vapnik, V.; and Vashist, A. 2009b. A new learning paradigm: Learning using privileged information. *Neural Networks*, 22(5): 544–557. Advances in Neural Networks Research: IJCNN2009.
- Wang, F.; Pan, J.; Xu, S.; and Tang, J. 2022. Learning discriminative cross-modality features for RGB-D saliency detection. *IEEE Transactions on Image Processing*, 31: 1285–1297.
- Wang, H.; Ma, C.; Zhang, J.; Zhang, Y.; Avery, J.; Hull, L.; and Carneiro, G. 2023a. Learnable cross-modal knowledge distillation for multi-modal learning with missing modality. In *International Conference on Medical Image Computing and Computer-Assisted Intervention*, 216–226. Springer.
- Wang, J.; Sun, K.; Cheng, T.; Jiang, B.; Deng, C.; Zhao, Y.; Liu, D.; Mu, Y.; Tan, M.; Wang, X.; et al. 2020a. Deep high-resolution representation learning for visual recognition. *IEEE transactions on pattern analysis and machine intelligence*, 43(10): 3349–3364.
- Wang, L.; Zhang, D.; Guo, J.; and Han, Y. 2020b. Image anomaly detection using normal data only by latent space resampling. *Applied Sciences*, 10(23): 8660.
- Wang, Y.; Peng, J.; Zhang, J.; Yi, R.; Wang, Y.; and Wang, C. 2023b. Multimodal industrial anomaly detection via hybrid fusion. In *Proceedings of the IEEE/CVF Conference on Computer Vision and Pattern Recognition*, 8032–8041.
- Wolsey, L. A.; and Nemhauser, G. L. 2014. *Integer and combinatorial optimization*. John Wiley & Sons.
- Wyatt, J.; Leach, A.; Schmon, S. M.; and Willcocks, C. G. 2022. Anoddpn: Anomaly detection with denoising diffusion probabilistic models using simplex noise. In *Proceedings of the IEEE/CVF Conference on Computer Vision and Pattern Recognition*, 650–656.
- Yan, X.; Zhang, H.; Xu, X.; Hu, X.; and Heng, P.-A. 2021. Learning semantic context from normal samples for unsupervised anomaly detection. In *Proceedings of the AAAI conference on artificial intelligence*, volume 35, 3110–3118.
- Yin, Y.; Shrivastava, H.; Zhang, Y.; Liu, Z.; Shah, R. R.; and Zimmermann, R. 2021. Enhanced audio tagging via multi-to single-modal teacher-student mutual learning. In *Proceedings of the AAAI conference on artificial intelligence*, volume 35, 10709–10717.
- Yoa, S.; Lee, S.; Kim, C.; and Kim, H. J. 2021. Self-supervised learning for anomaly detection with dynamic local augmentation. *IEEE Access*, 9: 147201–147211.
- Zavrtanik, V.; Kristan, M.; and Skočaj, D. 2024. Cheating Depth: Enhancing 3D Surface Anomaly Detection via Depth Simulation. In *Proceedings of the IEEE/CVF Winter Conference on Applications of Computer Vision*, 2164–2172.
- Zou, Y.; Jeong, J.; Pemula, L.; Zhang, D.; and Dabeer, O. 2022. Spot-the-difference self-supervised pre-training for anomaly detection and segmentation. In *European Conference on Computer Vision*, 392–408. Springer.